

EFFECTS OF LIFT DISTRIBUTION AND WING POSTURE ON THE STABILITY AND CONTROL OF TAILLESS AIRCRAFT

Michael R. de Kock[1], Barbara B. Huyssen[2] & Joachim R. Huyssen[3]

[1]University of Pretoria, South Africa, u19098082@up.ac.za
[2]University of Pretoria, South Africa, Barbara.huyssen@up.ac.za
[3]Council for Scientific and Industrial Research, South Africa, joachim.huyssen@up.ac.za

Abstract

In the search for alternative aircraft configurations, the Natural Dominant Configuration is proposed as an ideal configuration. The NDC can offer suitable lateral-directional stability and control characteristics without vertical wings. The polyhedral, polyswept wing posture provides the stability characteristics, and control can be achieved through dedicated in-flight modifications to the spanwise lift distribution. Here, we explore the effects of variations in wing posture and twist on these characteristics. This is done to test a development process for numerical prediction and experimental observation of the flight behaviour of wings of the NDC. This could be used to propose details for posture and twist, as well as the layout and use of controls, to achieve effective and efficient lift distributions together with good handling qualities for designs with specific applications of the NDC. Lateral-directional stability properties, such as Dutch roll and control responses, such as adverse yaw, were predicted using the panel method Flow5 by systematically varying the defining angles of the wing posture and twist. The elliptical lift distribution was used as a baseline against which the dynamic flight responses were compared for progressive deviations towards bell-shaped lift distributions. A suitable twist distribution was then committed to a remotely controlled model with adjustable posture angles for captive flight testing in a 7 m wind tunnel. The predictions were compared against measured flight responses to disturbances induced by flight controls. The predictions show useful agreement with the measurements, making their combination an effective development process in the study of the NDC.

Keywords: Captive-flight in wind tunnel; Dutch roll; adverse yaw; wing posture, lift distribution

Nomenclature

BSLD	Bell-Shaped Lift Distribution
CDC	Current Dominant Configuration
DOF	Degrees of Freedom
ELD	Elliptical Lift Distribution
ID	Inner Dihedral
IS	Inner Sweep
LD	Lift Distribution
NDC	Natural Dominant Configuration
OA	Outer Anhedral
OS	Outer Sweep
Re_{Root}	Wing Root Reynolds Number
C_n	Yaw moment coefficient
C_L	Total wing lift coefficient
C_{np}	Roll rate induced yawing moment coefficient
$C_{n\beta}$	Sideslip induced yawing moment coefficient
$C_{l\beta}$	Side-slip induced rolling moment coefficient
$C_{n\delta}$	Aileron induced yawing moment coefficient
ζ_d	Dutch roll damping coefficient
F_Y	Yaw oscillation frequency
λ_I	Inner Taper Ratio
λ_O	Outer Taper Ratio

1. Introduction

The aviation industry faces mounting pressure to curb its growing environmental impact, with aviation estimated to contribute 2.4% of global CO_2 emissions and a disproportionately large share of total radiative forcing when non-CO_2 effects are accounted for [1]. Increasingly stringent regulations have incentivised the search for aircraft configurations that offer efficiency improvements beyond what incremental development of the Current Dominant Configuration (CDC) can deliver [2]. The Natural

https://doi.org/10.71945/icas2026_0924

Dominant Configuration (NDC), proposed by Huyssen [3], is a tailless concept expected to offer better flight efficiency than comparable CDC-based aircraft. Jones and Donlan [4, 5] and others have extensively studied the stability and control challenges of tailless aircraft. The absence of a vertical tail means that directional stability and control, and the mitigation of adverse yaw, must be achieved entirely through wing geometry and control-surface allocation. The spanwise lift distribution may be a key design lever in this context, beyond the aero-structural benefits demonstrated in similar research [6, 7, 8, 9]. Bowers [10] demonstrated that a Bell-Shaped Lift Distribution (BSLD) produces proverse yaw under aileron deflection, a property with significant implications for tailless aircraft that cannot rely on a rudder. Huyssen demonstrated with one specific wing posture of the NDC that good longitudinal and lateral stability and control qualities could be provided solely by the wing [3]. However, the combined effect of polyhedral, polysweep, and lift distribution on lateral-directional behaviour had not yet been systematically characterised. In this paper, we investigate how variations in wing posture and lift distribution affect the lateral stability and control of an NDC aircraft using a combined numerical and experimental approach. A parametric numerical study was performed using Flow5 [11], employing a Taguchi orthogonal array method to analyse the response to several design variables [12, 13]. These predictions were assessed experimentally by captive flight of a remotely controlled model of the simulated design with adjustable polyhedral angles and a prescribed BSLD in a 7 m wind tunnel [14]. The numerical predictions and wind tunnel measurements are presented in parallel, allowing comparison of predicted and observed behaviour for the tested polyhedral configurations.

1.1 Background

The CDC is a configuration with a single slender central fuselage on a single central main wing, with an empennage that provides trim, damping, stability, and control. Separating functions among these three elements makes the configuration successful, but also imposes avoidable structural and aerodynamic penalties in the form of fuselage and tail drag, tail weight, and suboptimal central lift generation. The NDC is without an empennage. Instead, a stable lifting fuselage is mounted on a single central wing with a polyhedral and polyswept planform, shown in Figure 1. The wing must simultaneously satisfy all lift, trim, damping, stability, and control requirements, with the outer wing section serving the functions that the vertical and horizontal tail surfaces perform in the CDC. The variables defining the wing posture of the NDC wing used in this study are illustrated in Figure 1 and are defined as follows: Inner Sweep (IS) and Outer Sweep (OS) describe the aft sweep angles of the inner and outer wing sections, respectively. Inner Dihedral (ID) describes the upward inclination of the inner wing section, and Outer Anhedral (OA) describes the downward inclination of the outer wing section. These four angles constitute geometric design variables investigated in this study. The spanwise lift distribution (LD) is shaped by applying a spanwise twist and forms the fifth design variable. The Elliptical Lift Distribution (ELD) is used as a baseline, as it minimises induced drag by offering the best span efficiency [15, 6]. Departures from this baseline that progressively unload the wingtip, tending towards a Bell-Shaped Lift Distribution (BSLD), are of particular interest. The lift distributions explored in this study, intermediate between the BSLD and the ELD, are labelled 1, 2, and 3 in order of progressive loading of the tip, as shown in Figure 2.

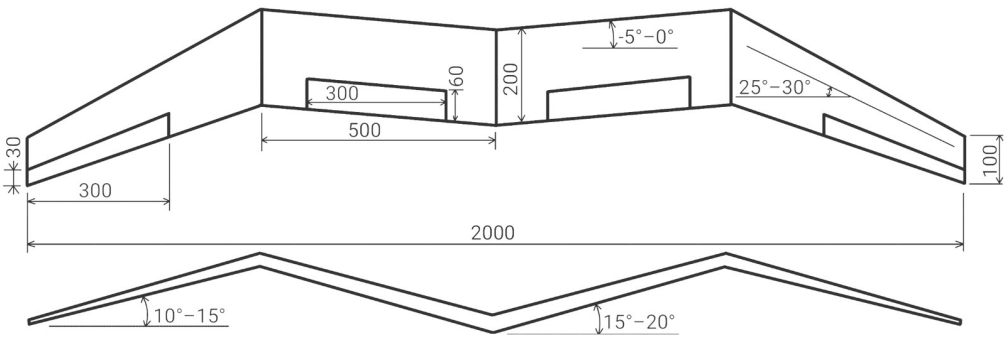


Figure 1 – The input geometric variables and ranges. All linear dimensions are given in millimetres. Inner and outer plain flap control surfaces are shown. Spanwise CAL4014I reflex airfoil [16].

2. Numerical Methods

We used the potential-flow solver Flow5 to simulate different wing postures of the NDC, with the geometry shown in Figure 1 and the operational conditions in Table 1. Viscous effects were estimated throughout to account for parasitic drag effects, though this is a limitation of the method. Table 2 shows the stability metrics of interest. The spanwise lift distributions investigated range from elliptical to bell-shaped, as shown in Figure 2, and were achieved using a non-linear spanwise wing twist, maintaining a linear downwash gradient and constant lift coefficient as per the optimal lift distribution results of Wroblewski [6]. The associated induced drag distributions are also displayed in Figure 2, where the presence of positive lift, upwash and resulting negative induced drag can be seen.

Table 1 – Operational conditions used for all simulations

Lift Coefficient (C_L)	0.42
Reynolds Number (Re_{Root})	175 000
Trimmed Flight Velocity	15 m/s

Table 2 – Stability derivative coefficients of interest

Side-slip induced yawing moment	$C_{n\beta}$	Side-slip induced rolling moment	$C_{l\beta}$
Aileron induced yawing moment	$C_{n\delta}$	Roll rate induced yawing moment	C_{np}
Dutch roll damping	ζ_d	Yaw oscillation frequency	F_Y

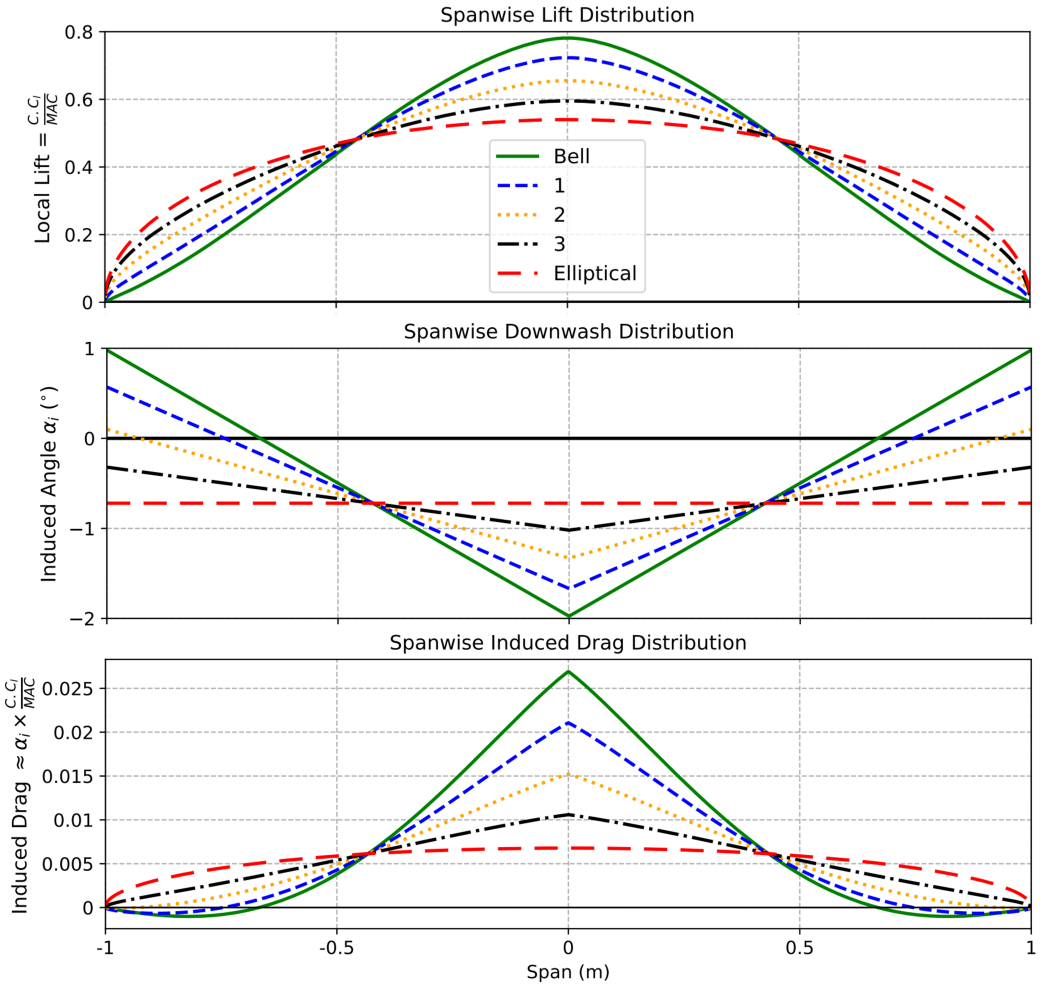


Figure 2 – Lift, downwash angle and induced drag distributions for the range of ELD to BSLD based on the work by Wroblewski [6].

2.1 Parametric Study Design

The parametric study was divided into two parts to investigate the bell- and elliptically-shaped ends of the lift distribution spectrum. Thus, the bell Taguchi array was designed with the BSLD set as the low setting and distribution 1 as the high setting, and the elliptical array was designed with distribution 3 as the low setting and the ELD as the high setting. This allows the lift distribution to be treated as an input variable, indicating a shift towards a more elliptical shape. Table 3 shows the geometries of each aircraft in the two Taguchi array studies. This analysis required hundreds of simulations and necessitated a fast method, such as Flow5, especially for providing trend information on external flow. The two arrays were normalised and compared to investigate how the input parameters affect the chosen output parameters across the lift distribution spectrum.

Table 3 – Taguchi orthogonal arrays used for the Bell and Elliptical lift distribution studies.

Aircraft	Geometry Parameters				Lift Distribution	
	OS (°)	IS (°)	OA (°)	ID (°)	Bell Array	Elliptical Array
1	25	-5	10	15	Bell	3
2	25	-5	10	20	1	Elliptical
3	25	0	15	15	Bell	3
4	25	0	15	20	1	Elliptical
5	30	-5	15	15	1	Elliptical
6	30	-5	15	20	Bell	3
7	30	0	10	15	1	Elliptical
8	30	0	10	20	Bell	3

The sensitivity parameter, or Taguchi effect, for each input and output variable is calculated using Equation 1:

$$\text{Effect of A on Z} = \text{A}_Z = \left(\frac{\sum H_A}{n_H} - \frac{\sum L_A}{n_L}\right)_Z \tag{1}$$

- H = sum of results at the high setting
- L = sum of results at the low setting
- n = number of trials.

2.2 Mesh Independence

A mesh independence study was performed to verify that the simulation results were independent of the panel density. The yawing moment coefficient ($C_{n\beta}$) at a sideslip angle of 15° was used because it is relatively sensitive to mesh density. Figure 3 shows the results and mesh used.
The results were considered independent of mesh density when successive changes were less than 0.5%. Mesh independence was achieved using 5800 panels, with stretching applied at the sweep joints, wingtips, and leading and trailing edges to improve resolution where high-pressure gradients were expected and to improve convergence.

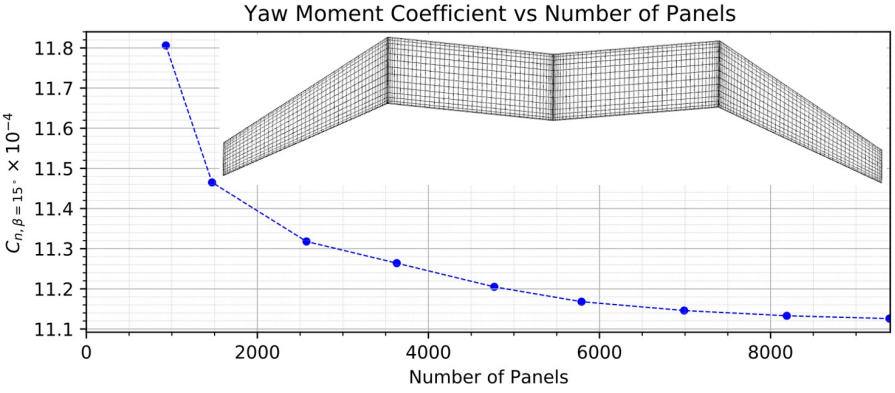


Figure 3 – Mesh independence study and mesh shown with 5800 panels.

3. Experimental Methods

We designed an experiment to further explore the stability and control of the NDC with a BSLD and adjustable polyhedral angles. The parametric study described in Section 2.1 was used to select the fixed design parameters of the physical model and identify the parameters of interest to vary, namely the aforementioned polyhedral angles. Wind tunnel-based captive flight testing was selected to investigate the aircraft's flight characteristics in a safe, controlled, and repeatable environment, without the risks associated with real-world free-flight tests. Captive-flight characteristics provide direct insight into an aircraft's true behaviour and its pilotablility, which is particularly important for early exploration of unconventional configurations such as the NDC, where practical flight behaviour and control implications are largely unknown. Such aircraft might behave quite differently from the CDC. We therefore designed and built a captive flight-testing rig to best represent free-flight conditions in a wind tunnel, allowing remotely controlled flight and enabling the aircraft to be arrested if control is lost. The setup also provides valuable pilot training for future flight tests.

3.1 Wind Tunnel Model

We performed the experiment using a single model based on the most favourable results of the parametric study, with the geometry shown in Figure 1. Table 4 shows the model's geometry.

Table 4 – Experimental Model Geometry

Lift Distribution (LD)	1	Inner Dihedral (ID)	5° to 15°
Inner Taper Ratio (λ_I)	1	Outer Anhedral (OA)	9° to 18°
Outer Taper Ratio (λ_O)	0.6	Inner Sweep (IS)	0°
Outer Sweep (OS)	30°		

We constructed the aircraft using laser-cut balsa and plywood for the ribs and fuselage, bonded to a tubular carbon fibre spar. The wings and fuselage surfaces were covered with 1-mm balsa and hot-melt adhesive film to create a smooth finish. The twist-and-sweep distribution was achieved using a laser-cut jig, ensuring accuracy and symmetry. The four wing sections and fuselage were joined using a double-pair friction plate hinge, manufactured from aluminium, that allowed the dihedral and anhedral angles to be adjusted between tests, as shown in Figure 5a. The centre fuselage section of the aircraft was enlarged to accommodate the electronics, movable ballast and gimbal, as shown in Figure 4.

Two sets of control surfaces, shown in Figure 1, were used to control the aircraft via a pilot-operated programmable radio transmitter. The outer surfaces (outer ailerons) served as elevons for pitch and roll control, and the inner surfaces provided lift augmentation and yaw control.

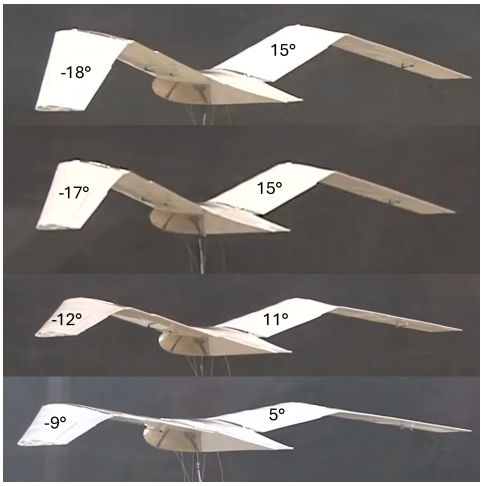


(a) (b)

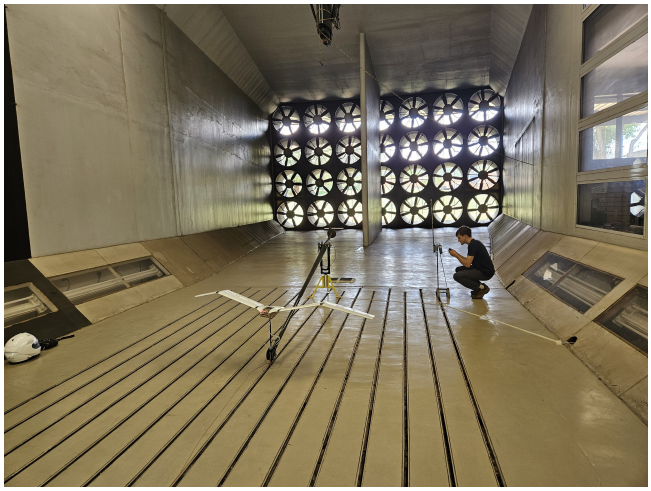
Figure 4 – (a) Adjustable ball joint gimbal to ensure that the CG and fulcrum always coincide at the trim condition (72 mm aft of the leading edge of the inner wing). (b) A carbon sting connects the ball joint to the captive rig via a set of bearings, allowing yaw freedom.

3.2 Test Facility

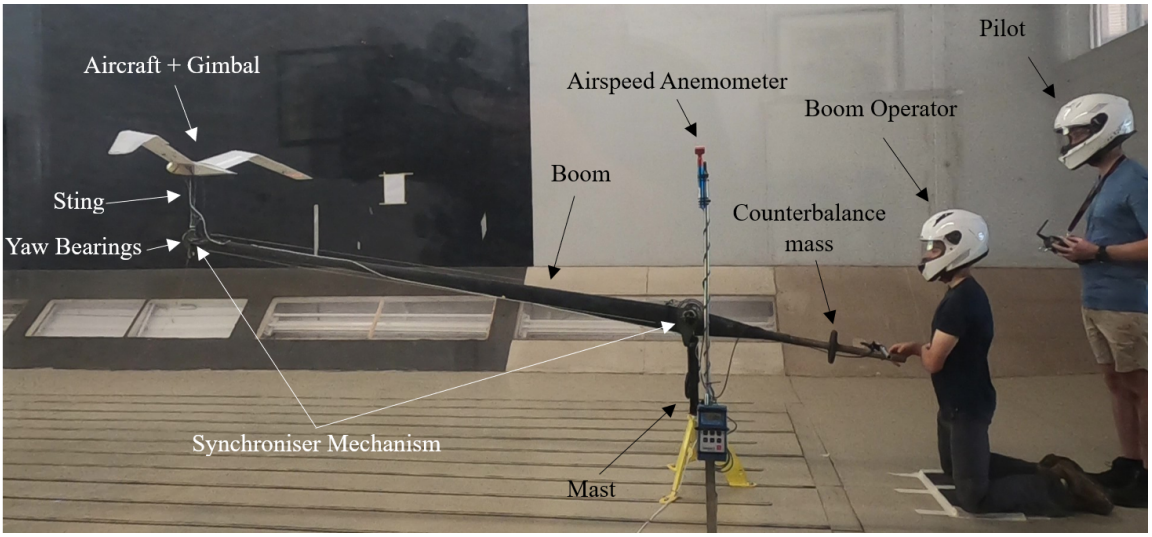
We performed the experiments at the Council for Scientific and Industrial Research [14]. Specifically, the 7-m wind tunnel was used, which allows a small aircraft to be flown within the tunnel's test section. The tunnel is continuous and open-circuit and is powered by 28 axial-flow fans (30 kW each). The airspeed is controlled by selecting one of 13 fan flow patterns, which allocate fan power and produce a uniform flow distribution with velocities ranging from 2 to 32 m/s in discrete steps. Speeds of 10, 12, and 15 m/s were consistently achieved and used for testing. The test rig for captive flight, shown in Figure 5c, was designed, constructed, and used to allow 5-DOF (Degrees of Freedom) flight within the wind tunnel. The rig constrains the aircraft along the wind axis via the gimbal mounted at the CG. This allows the aircraft freedom to roll, yaw, pitch, and translate laterally and vertically to investigate its stability, control and handling characteristics during flight. A 3-DOF (roll, yaw, and pitch) fixed-translation setup was used to investigate Dutch roll, yaw oscillation, and adverse-yaw responses without requiring pilot corrections that would disturb the aircraft's natural response. Onboard angular rate sensors (Adafruit NXP 9-DOF) and video recordings of position and angular offsets captured the aircraft's flight and control-surface movements. The consistency of the angular rate measurements was verified by displacing the aircraft about each axis and confirming the directions before each test. The measurements are only sufficient as a qualitative observational tool and cannot be used to determine stability derivatives or coefficients.



(a)



(b)



(c) Test rig video

Figure 5 – (a) Wing polyhedral configurations tested with the dihedral and anhedral angles annotated. (b) CSIR 7.5x6.5x13 m wind tunnel test section [14]. (c) Experimental setup for captive flight by remote control with boom and gimbal mass balanced such that the aircraft only lifts its mass.

4. Results and Discussion

4.1 Lateral-Directional Stability

Figure 6 displays the sensitivity of directional stability (C_{n_β}), dihedral effect (C_{l_β}) and yaw oscillation frequency (F_Y) to changes in the input parameters as calculated from the bell and elliptical Taguchi orthogonal arrays, shown in Table 3. C_{n_β} and C_{l_β} are indicative of lateral-directional static stability and are linked to Dutch roll behaviour and oscillation frequency. The yaw moment coefficient (C_n) was plotted against the sideslip angle (β) for the elliptical and bell lift distributions at two different outer anhedral angles (5° and 15°). The results are plotted in Figure 6d.

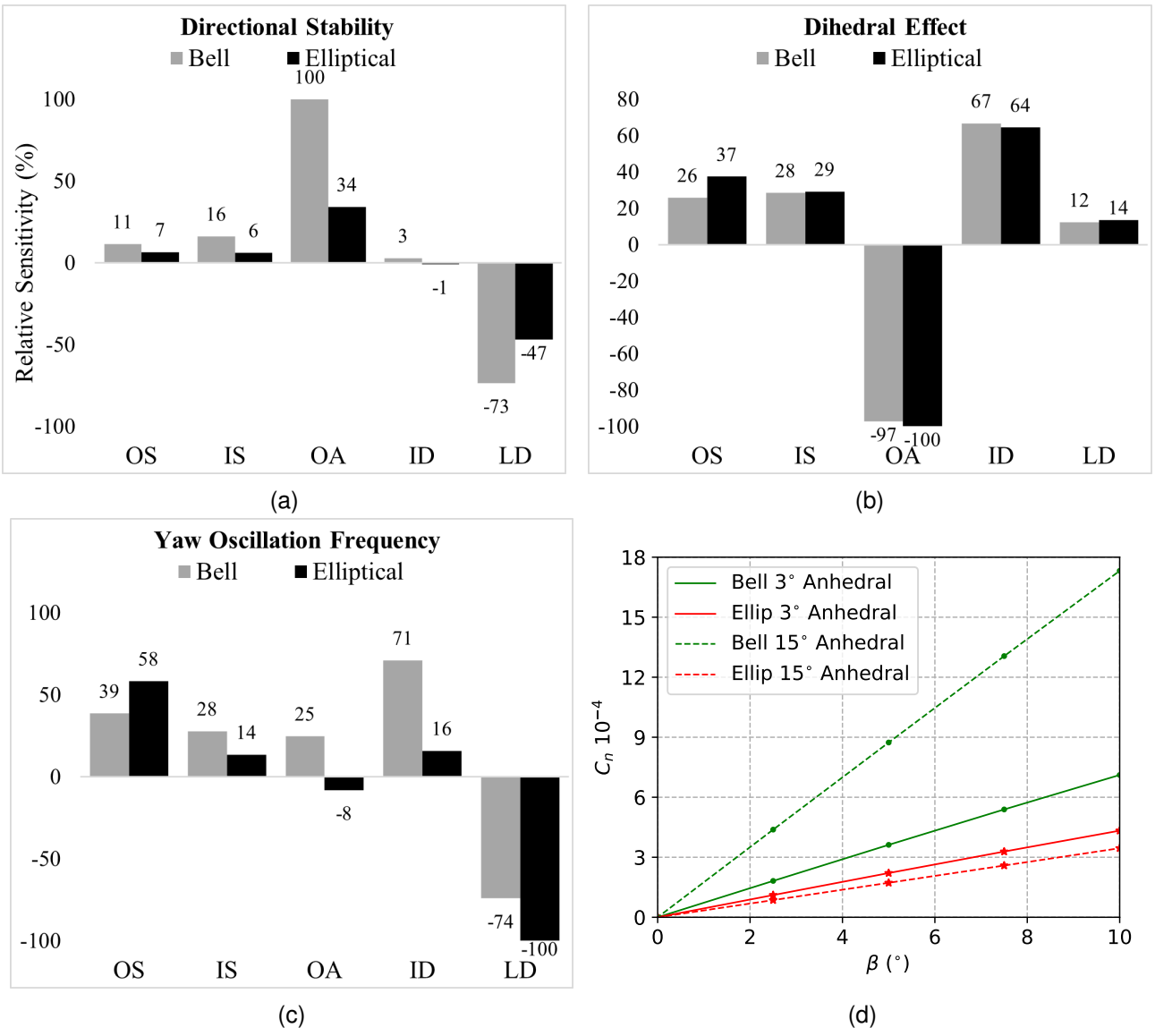


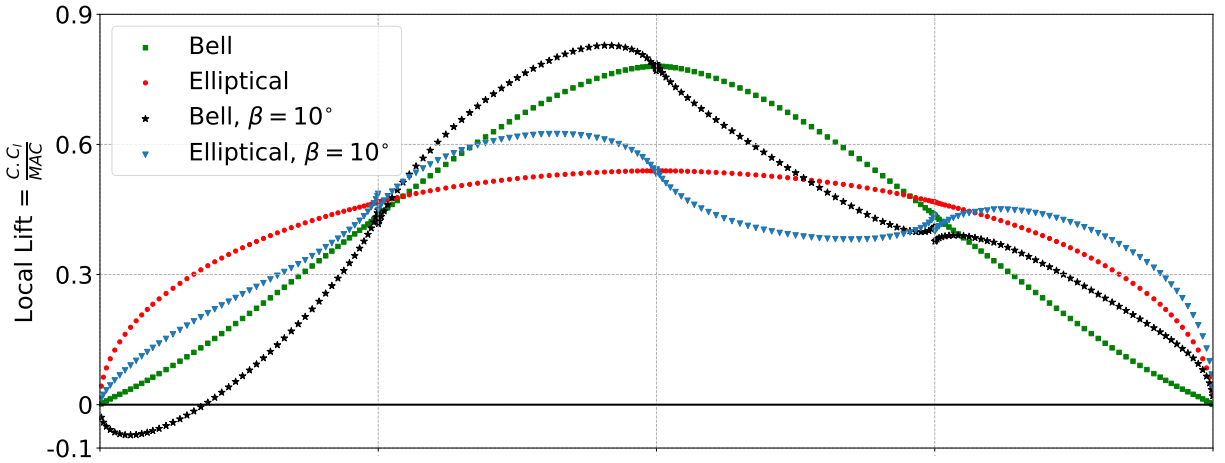
Figure 6 – Parameter sensitivity charts; (a) Directional stability (C_{n_β}), (b) Dihedral effect (C_{l_β}). (c) Yaw oscillation frequency. (d) Anhedral effect on directional stability, bell vs elliptical.

$C_{n,\beta}$ was most sensitive to changes in Outer Anhedral (OA) and Lift Distribution (LD), particularly for the Bell-Shaped Lift Distributions (BSLD), as shown in Figure 6a. This indicates a beneficial relationship between OA and the BSLD. Furthermore, on average, the BSLDs have 224 % greater directional stability than the elliptical lift distributions (ELDs) when comparing the averaged raw results of the two orthogonal arrays. This information may be significant for NDC, as directional stability is one of the most crucial factors for achieving good lateral handling qualities, as discussed in NASA's work on tailless aircraft [5],[4]. Less significant improvements in $C_{n,\beta}$ are also visible with the additional aft wing sweep, and Inner Dihedral (ID) is $C_{n,\ beta}$- invariant.

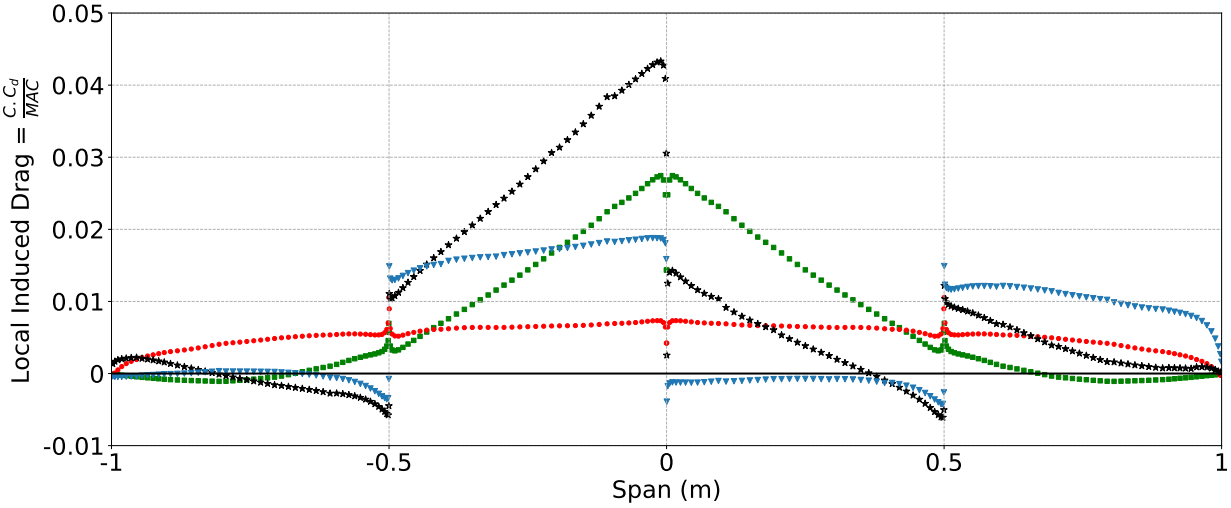
Examining Figure 6d, increasing the anhedral angle from 5° to 15° more than doubles the directional stability for the BSLD and, conversely, decreases the directional stability for the ELD. This indicates that outer anhedral is beneficial only with a BSLD. Yaw oscillation frequency (F_Y) is linked to directional stability (C_{n_β}), where a higher frequency indicates greater yaw stiffness. F_Y is most sensitive to changes in lift distribution, with the BSLD being beneficial. An aft sweep is also indicated as beneficial for both the BSLD and ELD. Interestingly, ID increases the frequency of the BSLD, though it shows no significant effect on directional stability. Outer anhedral increases the frequency of the BSLD and decreases ELD frequency, although sensitivity is relatively low. This may further indicate the relationship between OA and the BSLD.

$C_{l,\beta}$ was most sensitive to changes in the dihedral angles (ID and OA), as expected, with no notable change between the BSLDs and ELDs, as shown in Figure 6b. $C_{l,\beta}$ should be carefully controlled to be slightly negative (sideslip to the left causes a roll to the right) to ensure good lateral stability qualities and to prevent excessive yaw-roll coupling. The sweep angles had a less pronounced but notable effect, with aft sweep increasing the dihedral effect. The strong opposing effects of ID and OA suggest that the polyhedral angles can be tuned to achieve the desired dihedral effect.

The relationship between OA, LD, and $C_{n,\beta}$ was further explored using the spanwise distributions of lift and induced drag. Figure 7a shows how the BSLD and ELD are modified when forced into a side-slip to the left (nose yawed to the right) with 12° dihedral and 15° anhedral. Note that the dihedral angle was increased to allow for a neutral dihedral effect.



(a)



(b)

Figure 7 – (a) Change in spanwise lift for the elliptical and bell-shaped lift distributions due to a 10° sideslip to the left. (b) Corresponding change in induced drag distributions.

Figure 7a illustrates that the inner dihedral section of the wing experiences an increase in lift due to the local increase in angle of attack associated with the leading wing (left side) and a decrease in lift for the trailing wing (right side). The change in inner lift is fairly equal for the BSLD and ELD. The outer anhedral section experiences an opposite change in lift, effectively balancing the overall dihedral effect. However, the change in outer lift is more significant for the BSLD, particularly at the wing tip. The inner wing lift vectors are directed inwards and, as a result, generate a destabilising yaw moment (tends to increase the sideslip angle), whereas the outer wing lift vectors are directed outwards and generate a stabilising yaw moment (tends to decrease the sideslip angle). These opposing lift-induced yaw moments effectively cancel out, resulting in only a marginal increase in directional stability, which was also the conclusion of Donlan and Jones [5],[4].
The corresponding induced drag distribution, shown in Figure 7b, is modified according to the change in lift. The ID section shows a fairly equal and opposite drag change, where the leading wing (left) experiences an increase in drag and the lagging (right) wing experiences a decrease in drag, generating a stabilising effect, though minor, due to the short moment arm. The outer wing section shows a less significant change in drag, where the lagging wing increases in drag, causing a destabilising moment. The drag increase for the ELD, however, is more significant, causing a greater destabilising moment. The change in drag for the leading outer wing differs substantially between the ELD and BSLD: the ELD shows a decrease in drag, further destabilising the wing, whereas the BSLD shows an increase in drag towards the tip, generating a stabilising moment. These differences in the outer-wing induced-drag distributions likely account for the beneficial relationship observed between outer wing anhedral and the BSLD seen in Figure 6d.
The effect of polyhedral on directional stability was experimentally evaluated by measuring the model's yaw oscillation frequency in the wind tunnel as the polyhedral angles were varied. The yaw oscillation frequency is primarily governed by the yaw stiffness coefficient C_{n_β} and allows the trend in directional stability to be inferred. Figure 8 shows the simulated and experimental yaw oscillation frequencies and the correlation to directional stability.

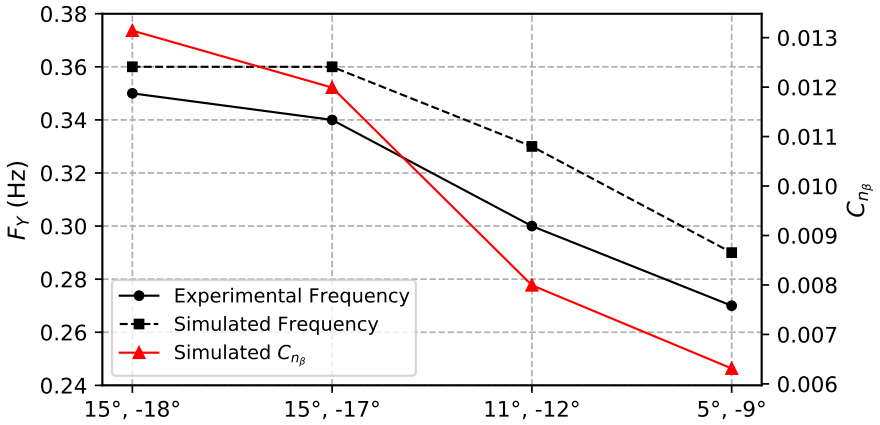


Figure 8 – Yaw oscillation frequency, simulation vs experimental and correlation to directional stability.

A strong correlation is evident in Figure 8 between the simulated and experimental yaw oscillation frequencies, with the simulated frequency consistently higher. This suggests that the experimental model likely has lower directional stability than the Flow5 prediction model. Nonetheless, the trend of decreasing frequency and, thus, decreasing directional stability as polyhedral angles are reduced is consistent with the parametric study and demonstrates a potential benefit to the polyhedral posture on the NDC.
In conclusion, the directional stability of the NDC was found to be improved by using a BSLD in combination with an anhedral outer wing section. The BSLD was superior to the ELD as it reduced the destabilising moment generated by the induced drag imbalance on the outer anhedral wing section during a side-slip.

4.2 Dutch Roll Behaviour

Figure 9 displays the sensitivity of Dutch roll damping (ζ_d) as determined from the numerical parametric study. ζ_d indicates lateral-directional dynamic stability and is linked to $C_{n,\beta}$ (Yaw stiffness) and $C_{l,\beta}$ (yaw-roll coupling).

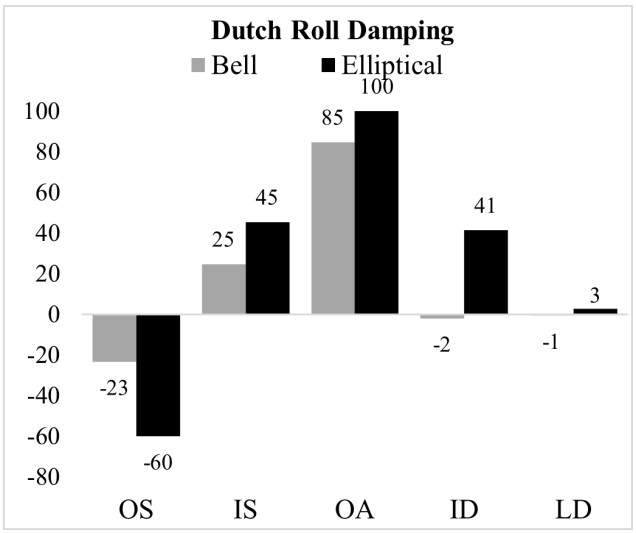


Figure 9 – Parameter sensitivity chart of Dutch roll damping.

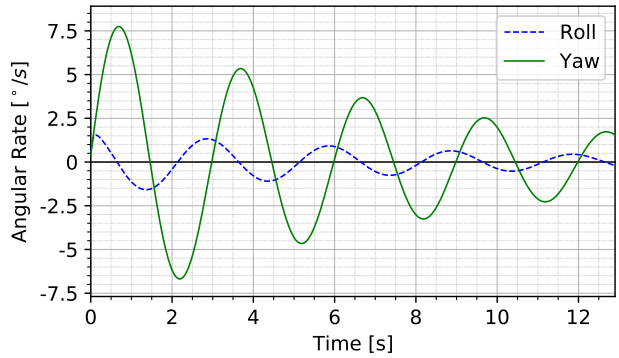
ζ_d is most sensitive to changes in OA, where greater anhedral corresponded with greater damping for both lift distributions, as shown in Figure 9. Sweep angles also mattered, with less-aft outer sweep and more-aft inner sweep improving damping. Interestingly, ID benefited the ELDs but showed no benefit for the BSLDs, whereas LD was ζ_d-invariant. This suggests that OA may be a viable method to increase damping and directional stability.

The effect of polyhedral on Dutch roll behaviour was experimentally evaluated by measuring the aircraft's yaw and roll rates in the wind tunnel when the aircraft was excited into Dutch roll mode by a sudden release at maximum yaw deflection. Figure 10 shows the simulated and experimental Dutch roll time responses of the aircraft from which the damping (ζ_d) and frequency (F_Y) are extracted, and yaw-roll coupling ($C_{l,\beta}$) can be visualised. Table 5 summarises the simulated vs experimental Dutch roll damping.

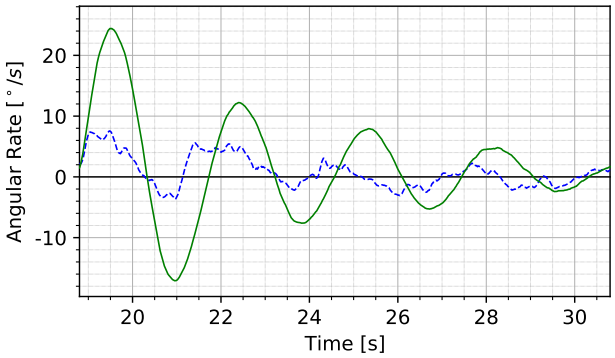
Table 5 – Dutch roll damping ratio, simulation vs experimental.

Configuration	Simulation	Experimental	
	$\zeta_{d,15m/s}$	$\zeta_{d,10m/s}$	$\zeta_{d,15m/s}$
15°, -18°	0.058	0.13	0.10
15°, -17°	0.049	0.12	0.11
11°, -12°	0.013	0.15	0.08
5°, -9°	-0.001	0.14	0.13

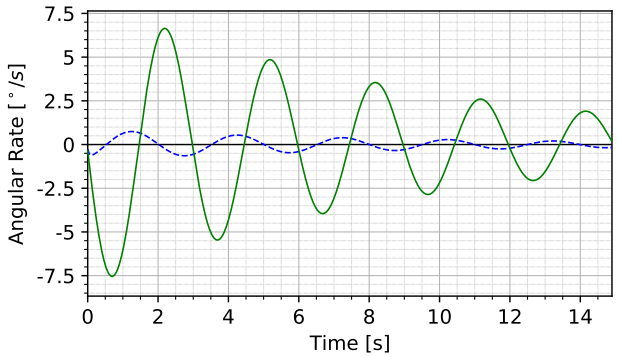
From Table 5, it is clear that there is a discrepancy between the simulated and experimental damping coefficients, with the wind tunnel model having significantly higher damping than predicted. Furthermore, the experimental damping is effectively polyhedral invariant. This suggests that Dutch roll damping is not dependent on the outer anhedral angle as was predicted in Figure 9. This might reflect a limitation of the potential flow method in capturing viscous damping, although further investigation is needed.



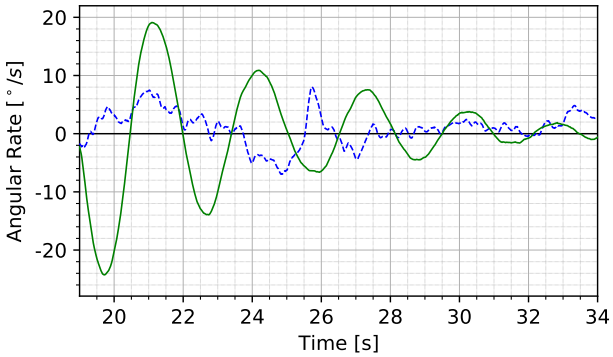
(a) Flow5 F_Y=0.36 Hz ζ_d=0.058 (15°, -18°)



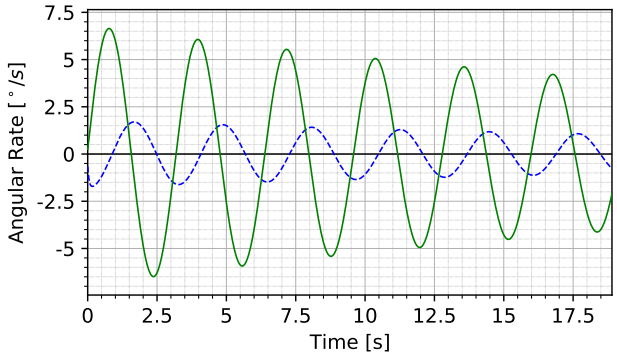
(b) Exp F_Y=0.35 Hz ζ_d=0.10 (15°, -18°)Video 6.2



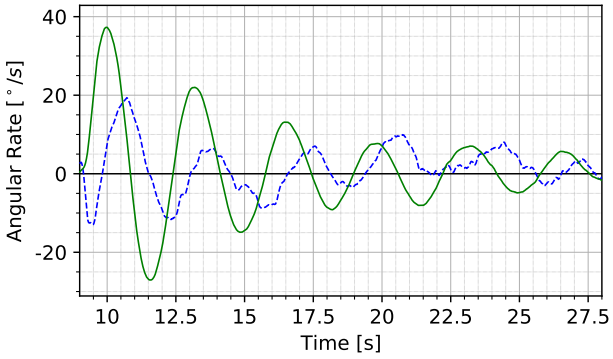
(c) Flow5 F_Y=0.36 Hz, ζ_d=0.049 (15°, -17°)



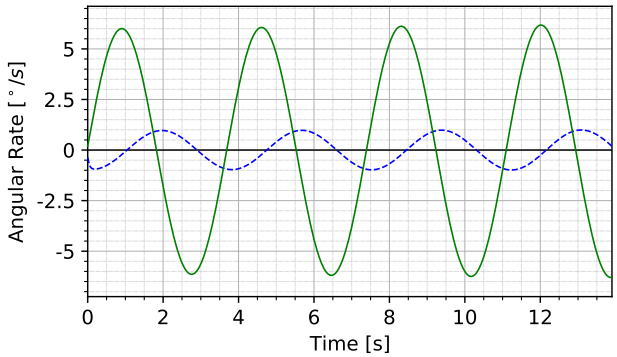
(d) Exp F_Y=0.34 Hz, ζ_d=0.11 (15°, -17°) Video 14



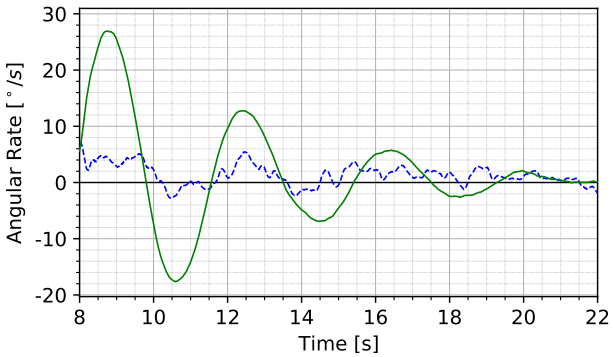
(e) Flow5 F_Y=0.33 Hz, ζ_d=0.013 (11°, -12°)



(f) Exp F_Y=0.29 Hz, ζ_d=0.08 (11°, -12°) Video 21



(g) Flow5 F_Y=0.29 Hz, ζ_d=-0.001 (5°, -9°)



(h) Exp F_Y=0.27 Hz, ζ_d=0.13 (5°, -9°) Video 29

Figure 10 – Simulated (left) and experimental (right) Dutch roll response at 15 m/s, for polyhedral angles: (a,b) 15°, -18° (c,d) 15°, -17° (e,f) 11°, -12° (g,h) 5°, -9°.

Despite the discrepancy in damping seen in Figure 10, good correlation between the simulation and experiment is evident in the coupling of roll to the dominant yaw oscillation. At 15°, -18°, Figures 10a and 10b, the model displays an opposite roll oscillation lagging 90° out of phase with the yaw, which

indicates an anhedral-dominant effect (sideslip to the right causes a roll to the right). By decreasing the anhedral to 17°, this effect is reduced significantly to the point where no anhedral effect is detectable in Figure 10d. At 11°, -12°, Figures 10e and 10f, the model displays a roll oscillation lagging 90° out of phase with the yaw in the same direction, which indicates a dihedral-dominant effect (sideslip to the right causes a roll to the left). This motion is familiar as the typical Dutch roll response when a dihedral effect is present and directional stability is low. The 11°, -12° configuration had the lowest damping, likely because strong yaw-roll coupling allows momentum to transfer between the roll and yaw axes, potentially reducing system damping. At 5°, -9°, Figures 10g and 10h, the aircraft displays a slight dihedral-dominant Dutch roll, which we predict to be the favourable condition, as it presents with virtually no roll oscillation and a damped yaw oscillation.
In conclusion, the yaw-roll response of the Dutch roll showed good correlation despite higher-than-predicted damping. The source of the discrepancy is not fully understood but may reflect limitations of the potential flow method in capturing viscous damping contributions. Furthermore, tuning the polyhedral ratio can reverse and cancel the Dutch roll response entirely, which appears necessary to improve damping and reduce roll oscillation.

4.3 Adverse Aileron Yaw

Figure 11 displays the sensitivity of adverse aileron yaw (C_{n_δ}), and adverse yaw due to roll rate (C_{n_p}). C_{n_δ} and C_{n_p} indicate lateral-directional control during rolling manoeuvrers.

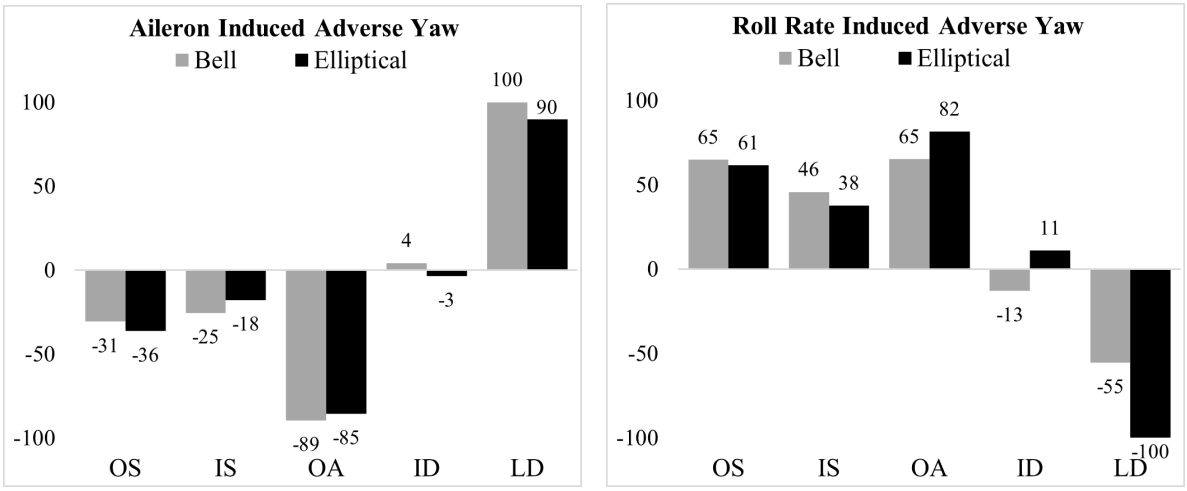


Figure 11 – Parameter sensitivity charts: (a) adverse aileron yaw, (b) adverse yaw due to roll rate.

C_{n_δ} was most sensitive to changes in LD and OA, with greater anhedral and a more bell-shaped distribution decreasing adverse aileron yaw, as shown in Figure 11a. Anhedral makes the aileron a semi-vertical, tip-mounted rudder aft of the CG, generating lift that produces roll and yaw moments in the same direction. Furthermore, examining the raw data from the Taguchi arrays, we find that the BSLDs always provided proverse aileron yaw, while the ELD provided adverse aileron yaw even at high anhedral angles. This indicates a potential control benefit of the BSLD and OA in removing adverse aileron yaw.
However, adverse yaw due to roll rate (C_{n_p}) responds oppositely with greater anhedral and a BSLD, increasing adverse yaw, as shown in Figure 11b. This suggests that a wing with a BSLD and OA wings will have counteractive moments in the form of proverse yaw due to aileron deflection and adverse yaw due to roll rate. However, this analysis does not make clear which effect dominates the motion. This behaviour is explored in Figure 13.
The relationship between AO, LD, and adverse aileron yaw was further explored using the spanwise distributions of lift and induced drag. Figure 12 shows how the BSLD and ELD are modified when the ailerons are deflected to induce a roll to the left with 12° dihedral and 15° anhedral.

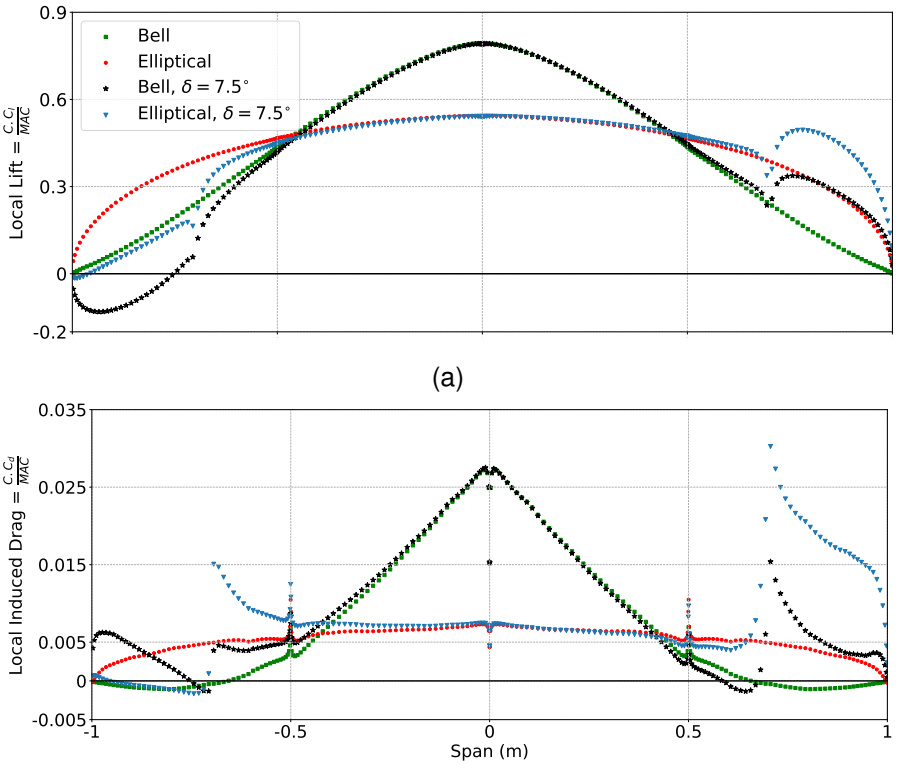


Figure 12 – (a) Lift and (b) induced drag distributions with ailerons deflected 7.5° in a right roll for BSLD and ELD.

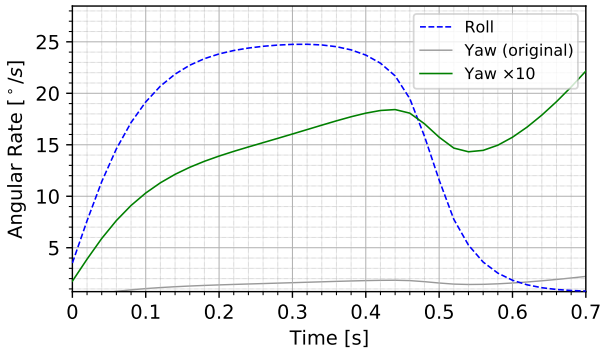
Figure 12a shows that the ELD generates a higher lift coefficient on the upgoing wingtip (right) when compared to the BSLD, for the same aileron deflection. This is associated with an increased risk of tip stall and possible control reversals at high α, particularly with swept and tapered wings. The BSLD, by contrast, requires negative lift on the downgoing wing, which increases the risk of lower-surface separation, particularly during pitching and rolling manoeuvres where large elevon deflections are possible. The differences in lift coefficients between the distributions affect the spanwise induced drag shown in Figure 12b.

Figure 12 illustrates the differences in aileron-induced drag for the BSLD and ELD. The ELD shows a significant increase in the induced drag generated by the down-going aileron (right wing) compared to the BSLD due to the higher lift coefficient. Furthermore, the ELD shows a decrease in induced drag from the upward aileron (left wing), whereas the BSLD shows an increase. The ELD therefore has a larger drag differential that generates a yawing moment opposite in direction to the applied roll and is likely responsible for the effect seen in Figure 11. The BSLD appears more balanced and generates proverse yaw due to the higher induced drag caused by the up aileron deflection and the lower induced drag generated by the down-deflected aileron.

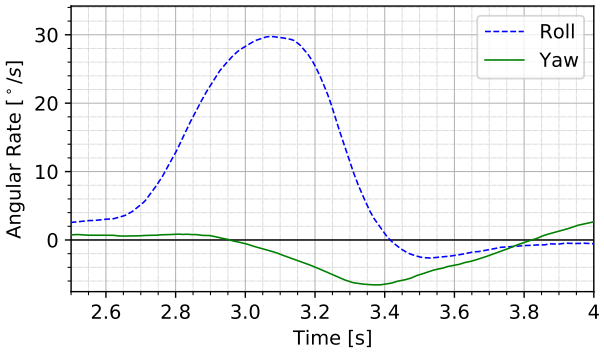
This analysis seems to contradict the explanation provided by Bowers et al. [10], where it was suggested that the proverse yaw effect, seen with the BSLD, is due to increased induced thrust generated by the down aileron. This does not appear to be the case, as the wingtip appears to be in a state of maximum induced thrust with no deflection. Any further increase in lift would result in added drag, as visible in Figure 12. The proverse yaw effect likely stems from the increased drag of the upward aileron. It should be noted that the ailerons are not optimised for proverse yaw, and the strength of the effect could likely be increased further by modifying the aileron geometry. Furthermore, the panel method was used only to estimate induced drag, as parasitic drag likely varies with design specifics, whereas induced drag is design-invariant provided a similar lift distribution. This means that the yaw predictions might differ in reality when the parasitic drag of an aileron is involved.

The effect of polyhedral on adverse yaw was experimentally evaluated by measuring the yaw and roll rates of the aircraft in the wind tunnel when the ailerons were deflected to induce a roll. Figure 13

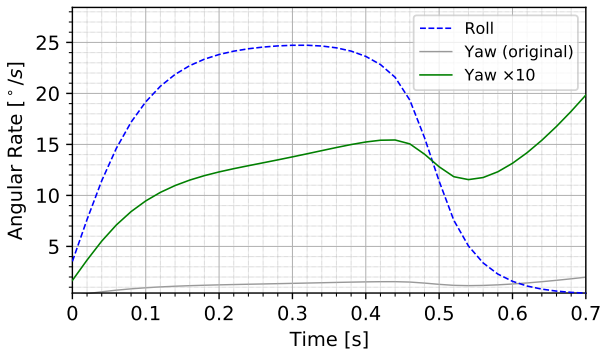
shows the simulated and experimental time responses of the aircraft. Note the use of a scaling factor for the simulated yaw rate to make the trend more visible.



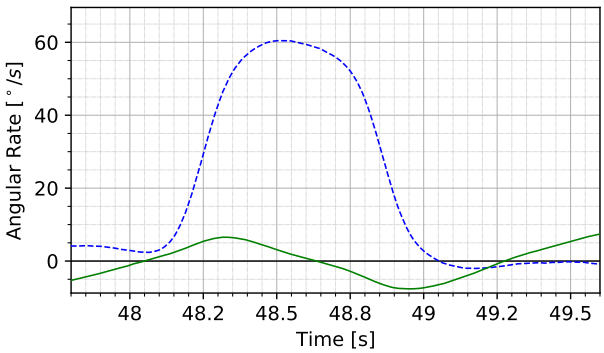
(a) Flow5 aileron response 15°, -18°



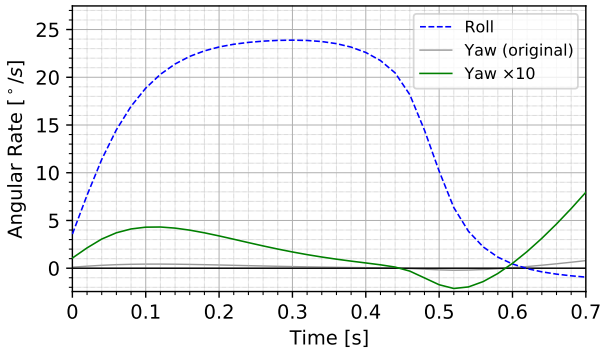
(b) Exp aileron response 15°, -18° Video 7.2, Pilot 7.2



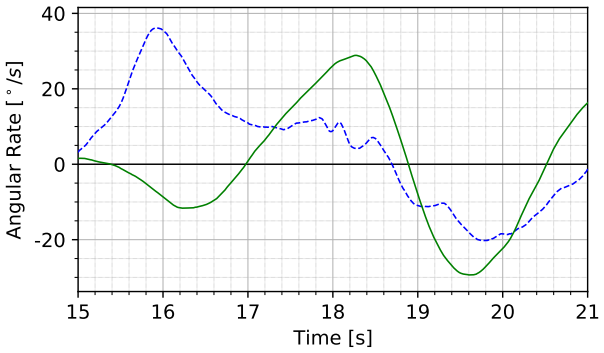
(c) Flow5 aileron response 15°, -17°



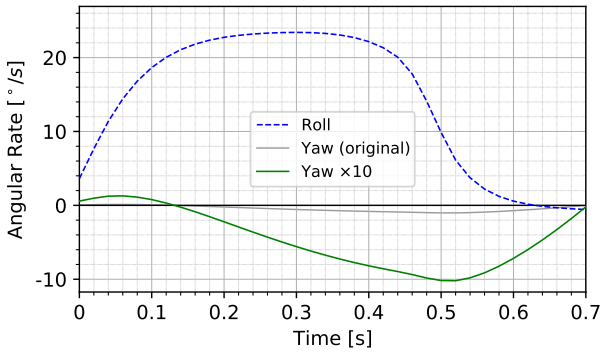
(d) Exp aileron response 15°, -17° Video 16



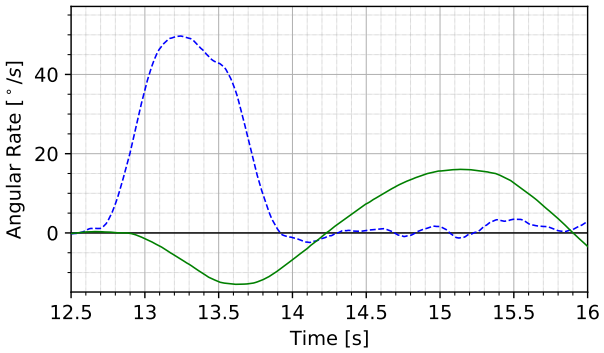
(e) Flow5 aileron response 11°, -12°



(f) Exp aileron response 11°, -12° Video 22



(g) Flow5 aileron response 5°, -9°



(h) Exp aileron response 5°, -9° Video 30

Figure 13 – Simulated (left) and experimental (right) aileron roll and yaw response at 15 m/s, for polyhedral angles: (a,b) 15°, -18° (c,d) 15°, -17° (e,f) 11°, -12° (g,h) 5°, -9°.

The simulations show that the 15°, -18° and 15°, -17° configurations have strong proverse yaw, particularly during the acceleration phase of the roll where aileron-induced yaw is dominant. As the roll rate increases, adverse yaw reduces the proverse yaw effect. When the ailerons are retracted, pronounced adverse yaw is evident at high roll rates. The 11°, -12° configuration shows an initial proverse yaw followed by adverse yaw as the roll decelerates. The 5°, -9° configuration shows slight proverse yaw in the acceleration phase of the roll, followed by adverse yaw thereafter. The simulations show that decreasing the polyhedral, and thus the outer anhedral angle, reduces proverse yaw.
The experimental model, however, exhibited significantly greater adverse yaw than the simulations predicted, predominantly during the high-roll-rate phase of the manoeuvre where roll-induced yaw dominates. However, some low level of proverse yaw is visible in the roll acceleration phase for the 15°, -17° configuration. No proverse yaw is apparent in the 11°, -12° and 5°, -9° configurations. This suggests that the aileron-induced proverse yaw, visible in the roll acceleration phase, is less pronounced in the experimental model than predicted, and that the roll-induced adverse yaw, visible during the high roll rate phase, is stronger than predicted. This leads to an overall more adverse yaw-prone configuration across the polyhedral range tested. The effect of lift distribution on adverse yaw is discussed in section 4.5, where the flaps were used to modify the lift distribution and test its effect on adverse yaw and the overall handling qualities of the model.

4.4 Yaw Control

Yaw control was achieved by deflecting the inner and outer control surfaces in opposite directions, as shown in Figure 15, with the four configurations in a maximal sideslip to the left (yaw to the right). This method of yaw control was proposed by Hainline et al. [17], where the aircraft (with a bell-shaped lift distribution) was equipped with inner and outer ailerons that deflected in opposite directions to generate a yaw moment and zero roll moment, by leveraging the proverse yaw of the outer ailerons and adverse yaw of the inner ailerons. Figure 14 shows the predicted induced drag distribution of the model with the yaw control flaps deflected in a yaw to the left.

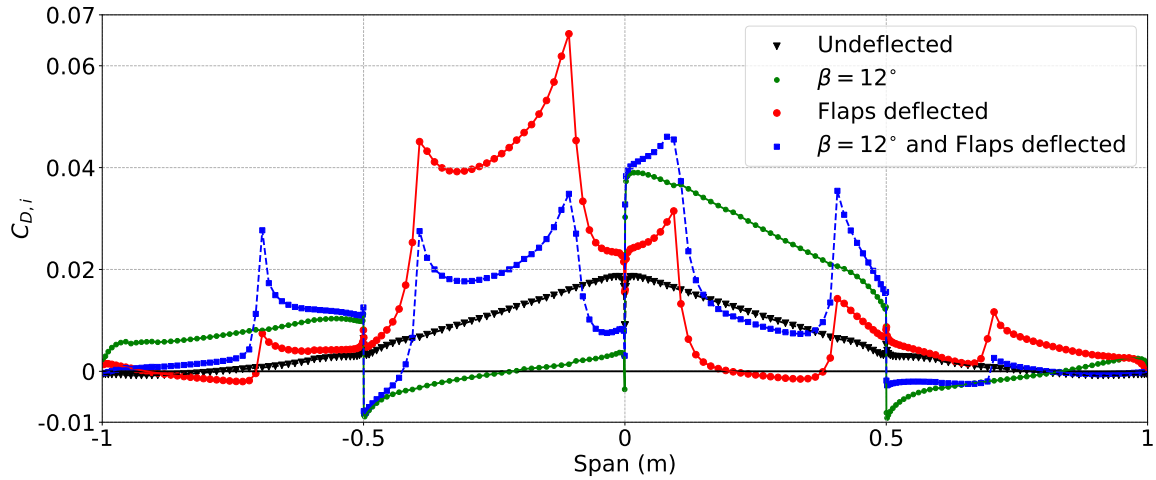


Figure 14 – Induced drag distribution associated with a left yawing manoeuvre, distribution 1, inner dihedral = 15°, outer anhedral = 17°. Inner ailerons at 15° (right), outer ailerons at 10° (left) achieve a stable yaw angle of 25° to the left.

To achieve a yaw to the left, the inner ailerons are deflected oppositely to generate a right roll, which creates a strong yaw moment to the left due to the adverse aileron yaw effect of the inner ailerons, as seen in Figure 14. The outer ailerons are simultaneously deflected in a left roll to cancel the roll moment of the inner ailerons. The outer ailerons have a minor proverse yaw effect and strengthen the yaw moment (to the left) as discussed in Section 4.3. The polyhedral configuration also strengthens this effect due to the inclination of the control surfaces. Figure 15 shows the experimental model when deflected in a yaw to the right using the yaw control system.

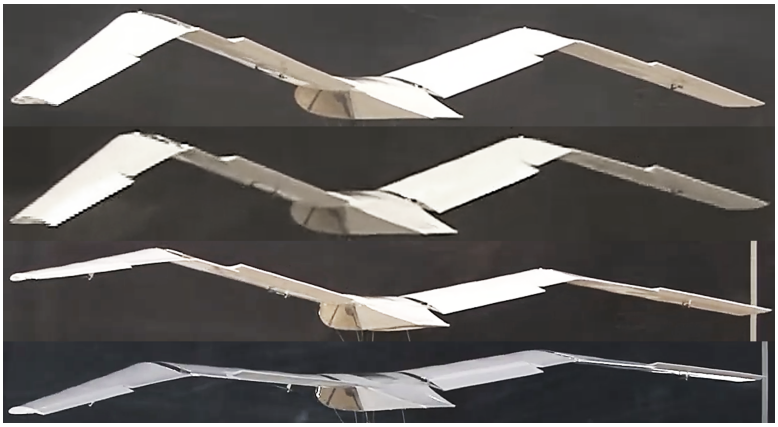


Figure 15 – A sideslip angle of approximately 15° achievable with all configurations. The following videos demonstrate the control Video 4.1, Video 4.1 Pilot (15°, -18°), Video 27.5 (5°, -9°).

Yaw control was mapped to the rudder input and tuned to ensure no roll output. This arrangement was effective and intuitive; however, the yaw response was relatively slow, likely due to the aircraft's low directional stability, and had less authority than predicted (15° vs 25°). The available control allowed any yaw oscillations to be stopped quickly by yawing into the oscillation and releasing the input in a controlled manner. This was possible because the yaw oscillation frequency was slow (less than 0.25 Hz), allowing the human response time (1 Hz) to easily counteract the oscillation. Yaw control was occasionally used to coordinate rolls in the wind tunnel as the model had adverse yaw. The pilot noted that it behaved similarly to a conventional aircraft in this regard and had ample yaw control to counteract the low levels of adverse yaw.

4.5 Lateral Handling Qualities

The handling qualities of the model were assessed using the 5-DOF setup, which allows the aircraft to translate under the pilot's control. The roll, yaw and pitch rates were measured to investigate flight dynamics and compare wing-angle configurations and flap settings across different flight velocities. Pitch stability was also tested since longitudinal stability is a prerequisite for flight, though the results are beyond the scope of this study. Figure 16 shows the predicted lift distributions of the experimental model at the design point (clean, 15 m/s), slow flight (elevons $\delta = -3°$, 12.5 m/s), slow flight with flaps (elevons $\delta = -2°$, flaps $\delta = +10°$, 12.7 m/s) and fast flight (elevons $\delta = +5°$, 29 m/s).

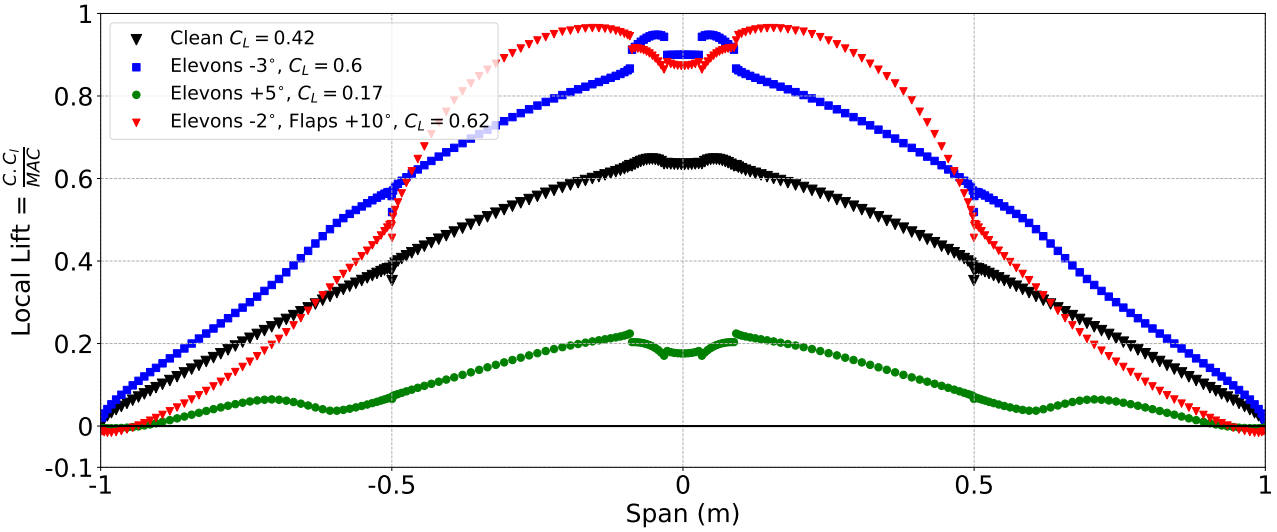
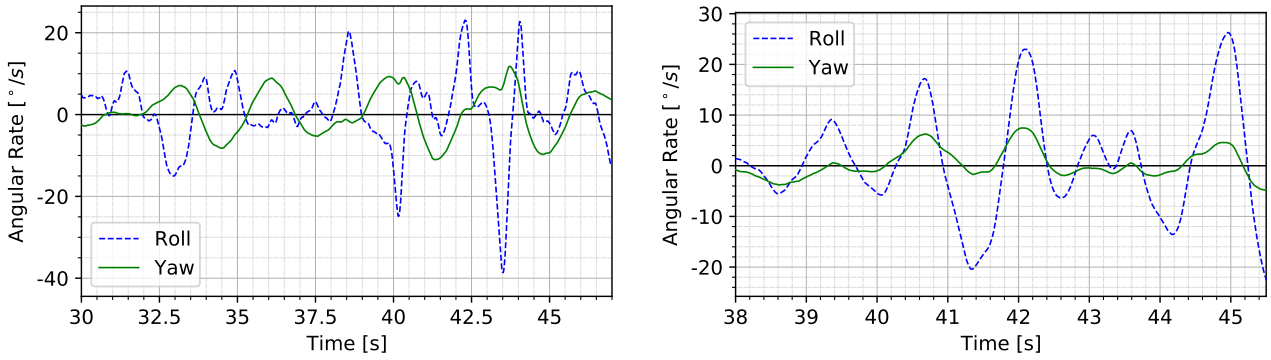


Figure 16 – Lift distribution for the simulated wind tunnel aircraft in the clean configuration (15 m/s, $\alpha = 0°$), with the elevons up (12.6 m/s, $\alpha = 2.4°$), the elevons down (26.2 m/s, $\alpha = -4.2°$) and with the flaps down and elevons up (12.4 m/s, $\alpha = -0.7°$).

Figure 16 shows how the lift distribution changes when the different control surfaces are deflected under steady flight conditions. Up elevator raises the nose, allowing the aircraft to trim at a slower speed and generating a higher lift coefficient across the wing. The up elevon provides a more bell-shaped lift distribution than the clean configuration. The down elevon lowers the nose and allows the aircraft to trim at a faster speed with a lower lift coefficient. The down elevon alters the lift distribution away from the prescribed bell shape.
Down flap deflection requires up elevon to trim the aircraft at a slow speed. This results in a slightly negative angle of attack relative to the clean condition. The flaps provide a significant increase in lift coefficient over the inner wing, though the up elevon and negative angle of attack decrease the lift coefficient over the tip section, suggesting little to no slow-flight benefit to the flaps. The flapped configuration results in an exaggerated bell-shaped lift distribution. A distinct loss in lift is evident over the fuselage area because the fixed fuselage airfoil is at a lower angle of attack with no added camber.
It is therefore expected that the slow-flight conditions, shown in Figure 16, should exhibit flight behaviour associated with a more bell-shaped lift distribution, due to flap and elevon deflections increasing the effective washout of the wing. Thus, slow-flight configurations should exhibit increased proverse yaw and directional stability.
Figure 19 shows the roll and yaw response of the experimental model in the 15°, -18° configuration at 15 and 10 m/s, respectively. Note that the experimental stall speed was lower than predicted, likely because the potential flow method cannot capture conditions with probable flow separation, such as at 10 m/s with full flaps.

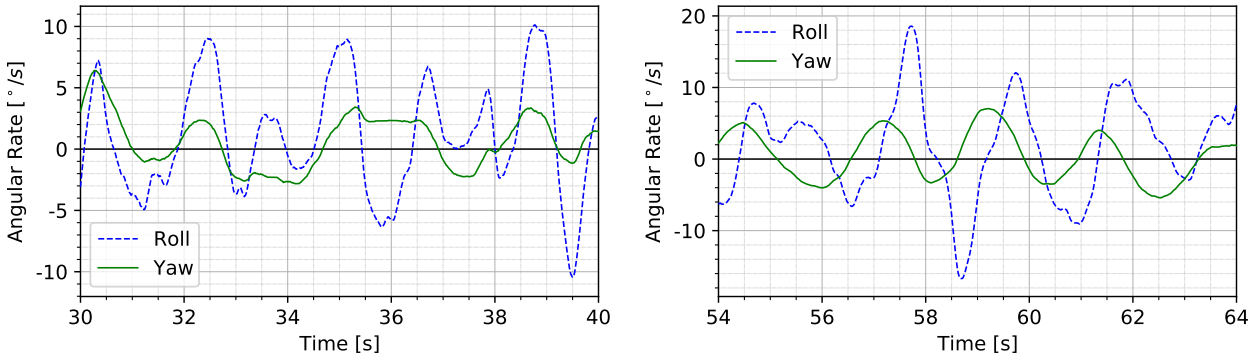


(a) 15 m/s, clean Video 1.2

(b) 10 m/s, Full flaps extended Video 1.1, Pilot 1.1

Figure 17 – Captive-flight time response at 15 and 10 m/s with flap, polyhedral 15°, -18°

Figure 17a shows a time response of the model at the design point (clean, 15 m/s), exhibiting a slow yaw oscillation, minor adverse aileron yaw, and minor proverse yaw visible during the acceleration phase of the roll manoeuvre (T = 42 s), which correlates well with the tests performed in Figure 13c. Figure 17b at 10 m/s with flaps shows a definite proverse yaw behaviour as the roll and yaw rates respond in synchrony. This contrasts with the tests performed at 15 m/s, where adverse yaw dominates. This suggests that the high-lift-coefficient setup (elevons up and flaps down) allows for proverse yaw due to the highly bell-shaped lift distribution as shown in 16. Figure 17b also appears to have increased directional stability and controllability due to the lack of yaw oscillations visible in the data. The pilot also noted increased directional stability and control.
Figure 18 shows the roll and yaw response of the 11°, -12° configuration at 12 m/s with flaps extended, and 15 m/s, clean, respectively.



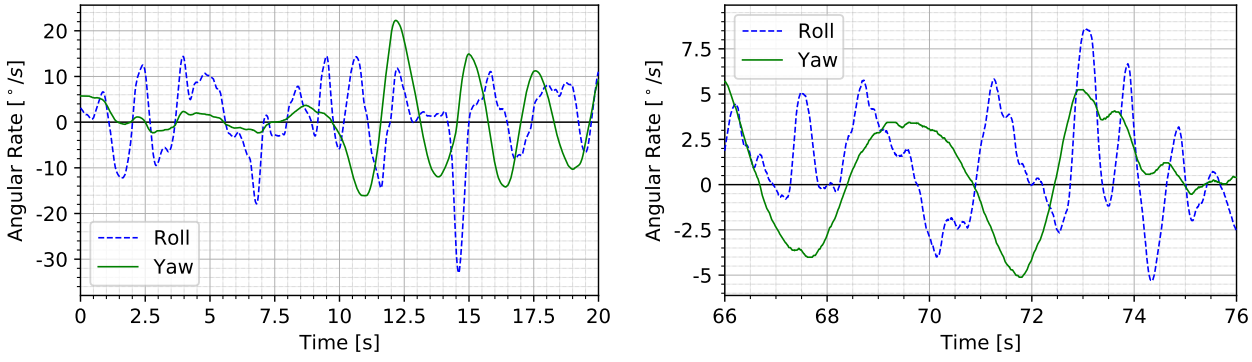
(a) 12 m/s Video 23

(b) 15 m/s Video 24

Figure 18 – Polyhedral 11°, -12° (a) 12 m/s, half flaps extended. (b) 15 m/s, clean.

Proverse yaw is evident in Figure 18a as the yaw rate mostly follows the roll rate. This again coincides with the use of flaps at low flight speeds. There does not appear to be any significant change in the proverse yaw effect measured when compared to Figure 17b at 15°, -18°, suggesting that aileron-induced yaw is independent of the anhedral angle. Figure 18b, at 15 m/s in the clean configuration, shows evidence of adverse yaw from 57 seconds, where the aircraft rolls and yaws in opposite directions. A Dutch roll oscillation is visible from 58 seconds onward. Pilot aileron input likely exacerbated the Dutch roll due to the adverse aileron effect, causing the aircraft to yaw further. The pilot noted less confidence in controlling this configuration, particularly at 15 m/s, where the flaps were not used. This was thought to be due to the dihedral effect and noticeable Dutch roll tendency, making it challenging to keep the aircraft centred in the tunnel.

Further tests were performed in which the flight velocity and/or flap configuration were changed during a single measurement to directly visualise the effects on the aircraft's motion. The time response for the 15°, -17° configuration at 15 m/s when the flaps are retracted is shown in Figure 19a, and the response of the 5°, -9° configuration as the flight velocity is decreased from 15 to 12-m/s is shown in Figure 19b.



(a) Flap effect at 15 m/s, 15°, -17° Video 16.2

(b) Flight speed effect (15 to 12 m/s, 5°, -9°), clean, Video 32.5

Figure 19 – Effect of flap and flight velocity at (a) 15°, -17° and (b) 5°, -9°

In Figure 19a, the flaps are extended for the first 10 seconds, which corresponds to proverse yaw and a well-controlled yaw axis. The retraction of the flaps at 10 seconds immediately triggers a yaw oscillation, as a left roll induces a right yaw. This suggests that directional stability was greatly reduced as the flaps were retracted, accompanied by increased adverse yaw. The pilot noted a significant reduction in controllability as the flaps were retracted, which is visible in Video 16.2. No yaw control was used during these tests. This effect was noticeable across the polyhedral range tested, as shown in Figure 19b at 5° and -9°, where the flight velocity was decreased from 15 to

12 m/s at 72 seconds. This velocity change corresponds with increased proverse yaw and improved directional stability. This behaviour can be linked to the lift distribution, as using the flaps corresponds to a more bell-shaped lift distribution. The proverse yaw and perceived improvement in directional stability when the flaps are extended correlate well with the numerical analysis, which shows that both proverse yaw and directional stability increase as the lift distribution becomes more bell-shaped. Stall and separation tests were performed on the 5°, -9° configuration using cotton tufts (Visible in Video 32.5). The stall speed was approximately 12 m/s without flaps, with separation starting at the wing root and never progressing beyond the inner wing section, even with full aft elevator, demonstrating good tip-stall prevention. Flap extension lowers the stall speed to approximately 10 m/s, with separation occurring across the flap span. No lower surface separation was observed on the outer elevons, even at full deflection, and a tip stall was never induced, despite the aircraft being fully stalled and rolling left to right. The gimbal limited nose-up pitch, and the aircraft could likely have achieved higher angles of attack without the gimbal limitation.

In conclusion, several valuable observations emerged from the captive-flight tests. These included proverse aileron yaw and improved directional stability when the flaps were extended and at low speed, compared to the clean configuration. Furthermore, the presence of a dihedral effect (in the 11°, -12° configuration) affected the aircraft's controllability due to excessive yaw-roll coupling. Finally, stall behaviour was controlled and predictable as tip stall was prevented, allowing roll control at all times.

5. Conclusion

In this study, we investigated the effects of spanwise lift distribution and polyhedral wing-posture variables on the NDC's lateral-directional stability and control through a numerical parametric study and a captive-flight wind tunnel experiment. The following conclusions are drawn.

Directional stability was most sensitive to outer anhedral and lift distribution. BSLDs provided more directional stability than ELDs across the parametric study, and the combination of outer anhedral and a bell-shaped distribution was mutually reinforcing. This relationship was confirmed experimentally, with the yaw oscillation frequency decreasing consistently as polyhedral angles were reduced, in agreement with the predicted trend. The numerical study found Dutch roll damping most sensitive to outer anhedral, with greater anhedral predicted to improve damping. Experimentally, damping was found to be significantly higher than predicted across all configurations and was effectively insensitive to changes in polyhedral angles. Roll-yaw coupling was well predicted, and balancing the inner dihedral and outer anhedral angles could eliminate Dutch roll by achieving a near-neutral dihedral effect. Adverse yaw was most sensitive to lift distribution and outer anhedral. The bell-shaped distribution consistently produced proverse yaw in the numerical study, while the elliptical distribution produced adverse yaw even at high anhedral angles. Experimentally, adverse yaw was more pronounced than predicted across all polyhedral configurations and was governed primarily by the lift distribution. Using flaps to increase effective tip unloading produced measurable proverse yaw and improved directional stability, confirming that lift distribution is the dominant driver of this behaviour. Yaw control was successfully demonstrated without a vertical tail by deflecting inner and outer control surfaces in opposition. A sustained sideslip of approximately 15° was achievable across all tested configurations, and the control arrangement was effective and intuitive.

The results suggest that a low polyhedral configuration, such as 5°, -9°, is sufficient to achieve acceptable lateral-directional behaviour provided a sufficiently bell-shaped lift distribution is maintained. Increasing the polyhedral angles beyond this offered no clear benefit to handling qualities, provided yaw-roll coupling remained low.

The combined tailoring of wing posture, lift distribution, and control-surface allocation is therefore a viable design strategy for achieving practical stability and control in tailless aircraft, demonstrated here through the concurrent use of Flow5 parametric simulation and wind-tunnel-based captive flight testing. Numerical simulation identifies promising geometric parameters and control strategies, while captive-flight testing validates predictions and reveals discrepancies that inform further refinement. This low-cost, closed-loop approach is well-suited to early-stage development of unconventional configurations such as the NDC, where flight behaviour cannot be reliably inferred from conventional design precedent.

6. Acknowledgements

The authors thank the Council for Scientific and Industrial Research (CSIR) [14] for generously providing wind tunnel facilities and technical support.

7. Contact Author Email Address

mailto: mrdekock4@gmail.com

8. Copyright Statement

The authors confirm that they and their organisation hold copyright in all of the original material included in this paper. The authors also confirm that they have obtained permission from the copyright holder of any third-party material included in this paper to publish it as part of their paper. The authors confirm that they give permission, or have obtained permission from the copyright holder of this paper, for the publication and distribution of this paper as part of the ICAS proceedings or as individual off-prints from the proceedings.

References

[1] Grobler C. *Past, present, and future climate impacts of aviation*. PHD Thesis, Massachusetts Institute of Technology, 2024.

[2] United Nations. For a livable climate: Net-zero commitments must be backed by credible action, 2023.

[3] Huyssen R J. *On the existence of a family of ideal aircraft configurations*. PHD Thesis, University of Pretoria, 2021.

[4] Jones R T. Notes on the stability and control of tailless airplanes. NACA Report, National Advisory Committee for Aeronautics, 1941.

[5] Donlan C. An interim report on the stability and control of tailless airplanes. NACA Report, National Advisory Committee for Aeronautics, 1944.

[6] Wroblewski G E and Ansell P J. Prediction and experimental evaluation of planar wing spanloads for minimum drag. *Journal of Aircraft*, 54(5):1664–1674, 2017.

[7] Verstraeten J G and Slingerland R. Drag characteristics for optimally span-loaded planar, wingletted, and C wings. *Journal of Aircraft*, 46(3):962–971, 2009.

[8] Klein A and Viswanathan S P. Minimum induced drag of wings with given lift and root bending moment. *Zeitschrift für Angewandte Mathematik und Physik*, 24:886–892, 1973.

[9] Jones R T. *The spanwise distribution of lift for minimum induced drag of wings having a given lift and a given bending moment*. National Advisory Committee for Aeronautics, 1950.

[10] Bowers A H, Murillo O J, Jensen R R, Eslinger B, and Gelzer C. On wings of the minimum induced drag: Spanload implications for aircraft and birds. NASA Technical Publication 2016–219072, National Aeronautics and Space Administration, 2016.

[11] Vic-Aéro. An analysis tool for planes and sails operating at low Reynolds numbers. `https://flow5.tech/`, 2026. Accessed: 2026-06-13.

[12] Unal R and Dean E B. Taguchi approach to design optimization for quality and cost: an overview. In *1991 Annual Conference of the International Society of Parametric Analysts*, 1991.

[13] Taguchi G and Wu Y. Introduction to off-line quality control systems. Technical Report, Central Japan Quality Control Association, Nagoya, Japan, 1980.

[14] Council for Scientific and Industrial Research. `https://www.csir.co.za/`, 2026. Accessed: 2026-05-26.

[15] Munk M M. The minimum induced drag of aerofoils. NACA Report, no. 121, National Advisory Committee for Aeronautics, 1923.

[16] Williamson G A, McGranahan B D, Broughton B A, Deters R W, Brandt J B, and Selig M S. *Summary of low-speed airfoil data*, volume 5. Department of Aerospace Engineering, University of Illinois at Urbana-Champaign, 2012.

[17] Hainline K, Richter J, and Agarwal R K. Vehicle design study of a straight flying-wing with bell shaped spanload. In *AIAA Scitech 2020 Forum*, page 0007, 2020. AIAA Paper 2020-0007.